SYNTHESIS AND DEPOSITION OF $BiVO_4$ THIN FILMS FOR PHOTODEGRADATION OF ORGANIC CONTAMINANTS

C. Sánchez García[1], *J. González Cuadra*[1], *J. Bautista Carda*[1]

[1]Department of Inorganic Chemistry, Universitat Jume I (UJI), Avenue Vicent Sos Baynat, s/n, 12006 Castelló de la Plana, Castelló, al395920@uji.es

Summary: The study focused on the formation and optimization of bismuth vanadate ($BiVO_4$) thin films for the photodegradation of organic contaminants, based on the production of reactive oxygen species (ROS). To optimize the films, a heterojunction with graphitic carbon nitride (g-C_3N_4) was created. Characterization techniques included X-ray diffraction (XRD), scanning and transmission electron microscopy (SEM and TEM), Ultraviolet-Visible spectroscopy (UV-Vis), Fourier transform infrared spectroscopy (FTIR), thermogravimetric analysis (TGA), and Raman spectroscopy. XRD results confirmed the monoclinic phase of $BiVO_4$ and that g-C_3N_4 does not affect its crystal structure. SEM and TEM revealed variations in film thickness and heterojunction formation. This study demonstrates the potential of $BiVO_4$ as a photocatalyst and highlights the importance of heterojunctions.

Keywords: $BiVO_4$, Thin films Photocatalysis, Heterojunction, Characterization techniques.

1. INTRODUCTION.

Water contamination is a global environmental issue that affects both human health and biodiversity. This situation is worsened by the discharge of pharmaceuticals, fertilizers, and pesticides into aquatic ecosystems, further exacerbated by industrial growth, intensive agriculture, and unregulated urban development. Although conventional decontamination methods exist, their effectiveness is limited, driving the search for more advanced and efficient techniques for wastewater treatment, such as Advanced Oxidation Processes (AOPs) and photocatalysis [1].

Photocatalysis, an emerging technique in contaminant treatment, uses semiconductor materials that, when irradiated with light, accelerate chemical reactions that break down contaminants into less toxic substances, such as water and carbon dioxide. This process is based on the generation of reactive oxygen species (ROS) that attack the pollutants. To improve the efficiency of semiconductors in these processes, techniques such as metal doping and the creation of heterojunctions are employed, which enhance charge separation and, consequently, contaminant degradation [2].

Bismuth vanadate is a promising semiconductor in photocatalytic applications, particularly in its monoclinic Scheelite phase, which exhibits high photocatalytic activity under visible light. This property allows for the degradation of organic compounds and hydrogen production through water splitting [3].

2. METHODOLOGY.

The methodology followed in the experimental procedure is based on the deposition of thin layers of $BiVO_4$ with different thicknesses using the spray pyrolysis deposition technique with a $BiVO_4$ liquid precursor. These layers are then optimized by applying g-C_3N_4 through the spin coating technique. Once the samples are optimized, they are characterized using various analytical techniques such as XRD, SEM, TEM, UV-Vis spectroscopy, FTIR spectroscopy, TGA and Raman spectroscopy.

3. EXPERIMENTAL PROCEDURE.

3.1. Materials and methods.

The $BiVO_4$ precursor was synthesized by dissolving $3 \cdot 10^{-4}$ mol of bismuth nitrate ($Bi(NO_3)_3$) in acetic acid (CH_3COOH) and $3 \cdot 10^{-4}$ mol of vanadyl acetoacetate ($V(acac)_2$) in ethanol (EtOH), and mixing them until homogeneity was achieved [4]. Thin layers of $BiVO_4$ were prepared with different volumes at a fixed concentration of 0.01M, as shown in Table 1, to optimize the appearance of the thin film. Different layer thicknesses were obtained by applying these various volumes, with the 4 mL sample, VA 1, selected as the optimum for this study.

Table1. Employed volumes to optimize the parameters.

Name of the $BiVO_4$ sample	Concentration of the precursor (M)	Concentration of the applied solution (M)	Total volume applied (ml)
VA 1	**0.01**	**0.0106**	**4**
VA 2	0.01	0.0105	6
VA 3	0.01	0.0107	8
VA 4	0.01	0.0105	12
VA 5	0.01	0.0104	15

For the deposition, 8 mL capacity atomizer with a fine grade of spraying connected to a compressed air pump at a pressure of 0.9 bar, is used, and thin coatings were manually deposited onto a glass (2.5 × 2.5 cm) previously heated to 500 ºC. Prior to heating, the glass was cleansed three times using ultrasonication for 10 min in water, EtOH, and acetone. Once applied, the sample is subjected to a calcination temperature of 550 °C on the hot plate during thirty minutes.

The C_3N_4 powder was synthesized using sodium nitrate ($NaNO_3$) and melamine in a 1:30 mol ratio as precursors [5]. The mixture was calcined through a controlled temperature gradient, consisting of a gradual increase to 500 °C, maintained for 120 minutes, followed by a rapid increase to 550 °C, also maintained for 120 minutes. Once synthesized, the C_3N_4 ink is prepared by dissolving 1 g of C_3N_4 in 5 mL of PEG 400 as a polymer, generating an ink that is applied using the spin coating method onto the previously applied $BiVO_4$ film, and his melting point is studied by TGA. The final films, containing 0.2 g of C_3N_4, were calcined again, producing the films used in the subsequent photodegradation experiments.

The thin films were used for the study of RhB photodegradation under UV light. A RhB solution of known concentration was prepared and kept in the dark to reach adsorption equilibrium. The degradation of RhB was monitored over time by analyzing concentration changes using UV-Vis spectroscopy at 550 nm. The degradation efficiency was calculated based on the initial and real-time concentrations of RhB. The photodegradation kinetics were evaluated using a reaction rate constant in the Equation (1).

$$k = \frac{-\ln\left(\frac{C}{C_0}\right)}{t} \quad (1)$$

where k (min^{-1}) represents the reaction rate constant at time t (min).

The reaction was monitored using a calibration curve constructed from standard RhB solutions. This process followed the Lambert-Beer equation, which relates the absorbance of a solution to the concentration of the absorbing species, allowing for precise measurements of RhB degradation efficiency over time, Equation (2).

$$\eta(\%) = \left(1 - \frac{C_t}{C_0}\right) \cdot 100 \quad (2)$$

where C_0 represents the initial RhB concentration and C_t represents the real time concentration of the contaminant.

4. RESULTS AND DISCUSSION.

4.1. XRD characterization.

After the application of the $BiVO_4$ layers, an XRD analysis of the films (Fig. 1) is conducted to verify that the crystalline structure remains unaffected despite variations in the application volumes, allowing the optimization of the $BiVO_4$ 0.01M volume. Once applied, the crystallinity is examined after adding the C_3N_4 ink (Fig. 2).

In Figure 1 a comparison of the crystalline structure of $BiVO_4$ is shown. As observed all the diffraction peaks are located in the characteristic peaks of monoclinic Scheelite $BiVO_4$ phase; 18.8 º, 28.9 º, 30.5 º, 34.55 º, 35.15 º, 39.9 º, 42.5 º, 45.9 º, 46.9 º, 47.3 º, 50.2 º, 53.45 º, 58.5 º, 59.8 º that correspond to the crystallographic planes associated with the miller index: (110), (-121), (040), (200), (002), (211), (051), (132), (240), (042), (202), (161), (170), (071) [33]. These values are given in the International Centre for Diffraction Data (ICDD) Card No. 14-0688 (space group I2/a, a = 5.195 Å, b = 11.701 Å, c = 5.092 Å, and β = 90.38 º).

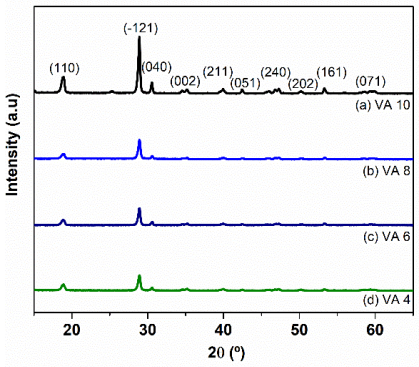

Figure 1. XRD comparison of different applied volumes of $BiVO_4$ 0.01M; (a) 10 mL, (b) 8 mL, (c) 6 mL, (d) 4 mL.

Figure 2 shows that the characteristic peaks of $BiVO_4$ are the same peaks of the $BiVO_4$ – C_3N_4 film, this is due to the smaller X-Ray scattering of the C_3N_4, in comparison with the $BiVO_4$.

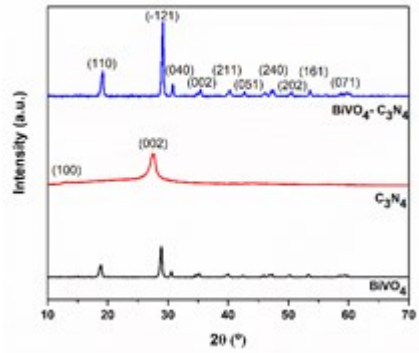

Figure 2. XRD comparison of films $BiVO_4$, $BiVO_4$ – C_3N_4 and C_3N_4 powder.

4.2. SEM analysis.

To analyze the morphology and composition of the applied layers, a study using SEM is carried out. This equipment, when coupled with Energy Dispersive X-ray Spectroscopy (EDX) detectors, allows for the determination of the presence and distribution of elements within the layers of the sample.

The surface morphology of the layer is studied (Fig. 3). The Image a) shows a view of the $BiVO_4$ – C_3N_4 film as seen from above and scanned with the secondary electron method of the SEM equipment. In the image, particles which are C_3N_4, are observed on the top of the film in a 100 µm scale. Image b) shows another view of the $BiVO_4$ – C_3N_4 film, as seen from above and scanned this time with the compositional method of the SEM equipment. This method allows the mass differentiation of the components. Consequently, heavier components, which have more electrons in the structure, in this case C_3N_4, appear on a darkest shade than the lighter components, $BiVO_4$, in a 100 µm scale. Lastly, Image c)

represents a C_3N_4 particle in a 100 nm scale, where the grouping of the C_3N_4 sheets is clearly visible.

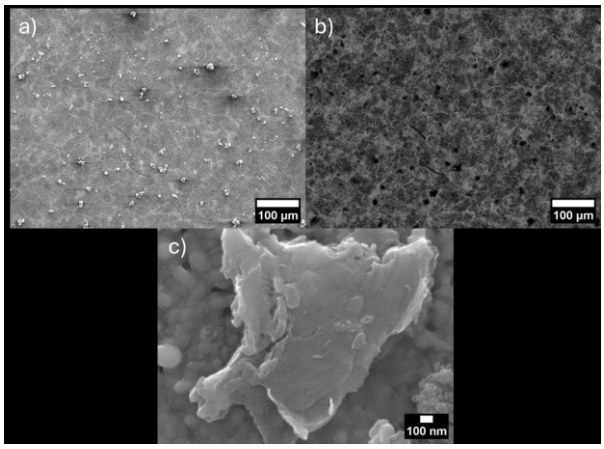

Figure 3. SEM micrograph of a) top surface of a $BiVO_4$ – C_3N_4 film analysed with secondary electrons method; b) top surface of a $BiVO_4$ – C_3N_4 film analysed by compositional method; c) C_3N_4 particle.

Subsequently, in Figure 4 the different compositions of the layer formed on the surface and the bottom of the film are analyzed via EDX, concluding that in Image a) the main components of the upper part of a glass surface layer sample are carbon and nitrogen. These components belong to the C_3N_4 molecule deposited on the top layer by the spin coating method. In Image b), the main components of the lower part of a glass surface layer sample are oxygen, vanadium, bismuth, and silica. These components, belong to the $BiVO_4$ molecule deposited on the bottom layer. Additionally, in both analysis trace amounts of the following components (Bi, V, O) originating from $BiVO_4$, and residual elements characteristic of the glass (Si, Ca, Na), can be observed.

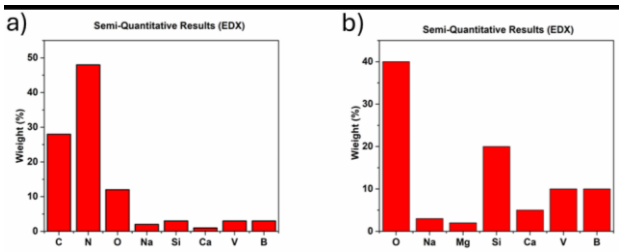

Figure 4. EDX spectra composition of the a) upper part of the thin film b) lower part of the thin film.

4.3. TEM analysis.

TEM is employed to analyze the detailed internal structure of the different materials of the thin films at the nanometric scale, enabling crystallographic, morphological, and compositional analysis of the sample.

In Figure 5, various HRTEM, High Resolution Transmission Electron Microscopy, images of g- C_3N_4 are presented. Image a) has a resolution of 10 nm, where a sheet of g- C_3N_4 can be observed. Conversely, in Image b), measured at a lower resolution of 200 nm, this graphitic sheet appears folded, showing the presence of wrinkles.

Image c) represents the Electron diffraction patterns obtained by the application of the Fourier transformation of HRTEM images (Images b) and c)). The comparison between the theoretical and experimental interplanar distances of C_3N_4 reveals that the unique observable ring is associated with the (200) crystallographic plane. This indicates a low crystallinity of the powder, as it is an organic compound that tends to have an amorphous structure.

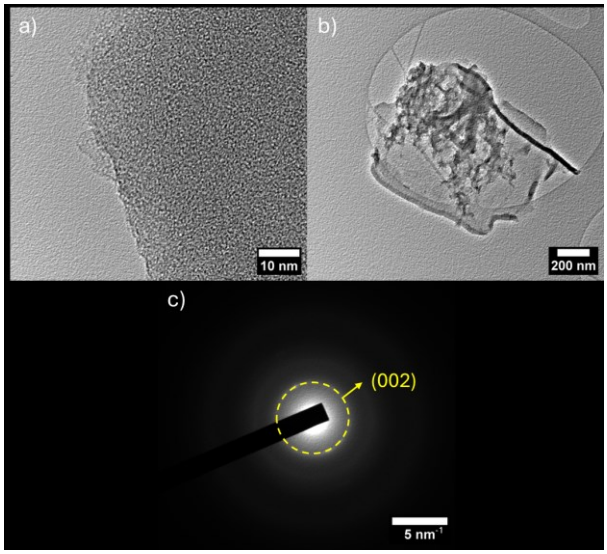

Figure 5. HRTEM micrograph of the nano-sized g-C_3N_4 powder with different resolutions a) 10 nm b) 200 nm and c) Electron diffraction patterns of the g- C_3N_4

4.4. UV-Vis spectroscopy.

The reflectance (R%) of the layers is measured using UV-Vis spectroscopy to determine the band gap of $BiVO_4$. In Figure 6, a reflectance spectrum of the $BiVO_4$ and $BiVO_4$-C_3N_4 films is presented.

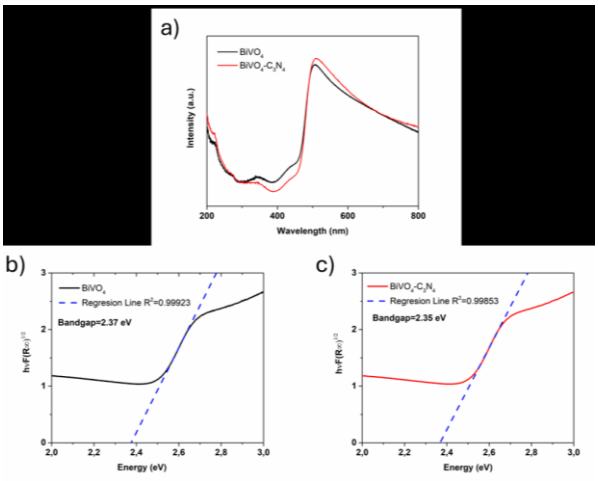

Figure 6. Optical characteristics of the $BiVO_4$ and $BiVO_4$-C_3N_4 thin films a) Reflectance spectra employing UV-Vis spectroscopy. Determination of the energy Band Gap though the Tauc plot of b) $BiVO_4$; c) $BiVO_4$-C_3N_4.

In Images b) and c), the Band Gap is estimated, due to the charge transfer between the VB and CB. As shown in Image b), the estimated value of the Band Gap for

$BiVO_4$ is 2.37 eV, and in Image c), the estimated value of the Band Gap for $BiVO_4$-C_3N_4 is 2.35 eV. A light decrease in the Band Gap can be observed.

4.5. Photocatalysis measurements.

Figure 7 exhibits the photodegradation of a RhB solution under various conditions: the addition of a $BiVO_4$ film as a photocatalyst, the addition of a $BiVO_4$-C_3N_4 film as a photocatalyst, and the solution without a photocatalyst. In Image a), the C/C_0 curve of RhB is presented, showing a significant improvement in photodegradation when g-C_3N_4 is applied to the bismuth vanadate layer. In Image b) the -Ln C/C_0 values are plotted, and the reaction rate constants are calculated by the Equation (3), as a result of solving the linear equations for each reaction. Indicating that the fastest photocatalytic reaction occurs with the $BiVO_4$-C_3N_4 film, which has a rate constant of k = 0.0033 min^{-1}. Image c), shows the decrease in absorbance of the RhB solution over time when using the $BiVO_4$-C_3N_4 film, revealing a noticeable decline between measurements. Image d) compares the degradation efficiency percentages in the three studied degradations, highlighting the efficiency of the $BiVO_4$-C_3N_4 film with a percentage of degradation of the 91 %.

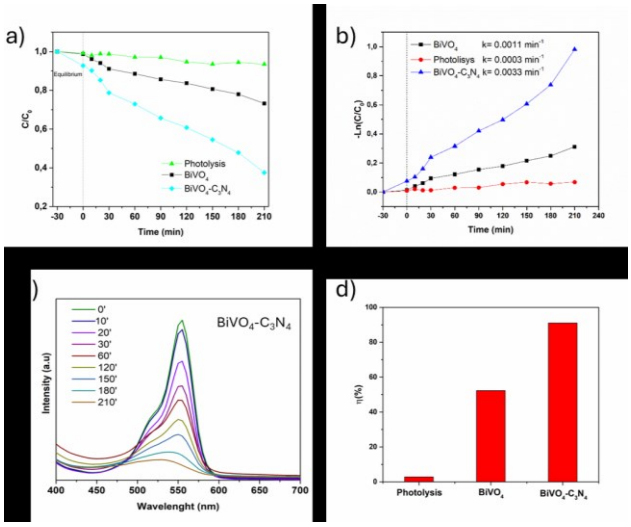

Figure 7. Photocatalytic degradation of a RhB solution under visible light illumination. Time-course variation of a) C/C_0 and b) -Ln(C/C_0) in photolysis and employing different photocatalysts. c) Time-course degradation using a $BiVO_4$-C_3N_4 thin film. d) Comparison of the degradation percentage in photolysis and employing different photocatalysts.

When exposed to UV-Vis light, $BiVO_4$ can absorb photons and generate electron-hole pairs, which can react with oxygen molecules, leading to the formation of superoxide radicals (O_2-·) and hydroxyl radicals (OH·). When a heterojunction is formed by coupling two semiconductors, such as bismuth vanadate (n-type semiconductor) and graphitic carbon nitride (p-type semiconductor), the electron-hole pairs are separated at the junction. The following reactions, occur as a result:

$$BiVO_4/g-C_3N_4 + hv_{VIS} \rightarrow BiVO_4(e^- + h^+) + g-C_3N_4(e^- + h^+) \quad (3)$$

$$BiVO_4(e^- + h^+) + g-C_3N_4\ (e^- + h^+) \rightarrow BiVO_4(e^-) + g-C_3N_4\ (h^+) \quad (4)$$

$$BiVO_4(e^-) + O_2 \rightarrow O_2^-\bullet + BiVO_4 \quad (5)$$

$$O_2^-\bullet + Pollutant \rightarrow CO_2 + H_2O \quad (6)$$

$$H_2O + hv_{VIS} \rightarrow H^+ + OH^- \quad (7)$$

$$g-C_3N_4\ (h^+) + OH^- \rightarrow OH\bullet + g-C_3N_4 \quad (8)$$

$$OH\bullet + Pollutant \rightarrow CO_2 + H_2O \quad (9)$$

These reactions allow the partial degradation of Rhodamine B into H_2O, CO_2, and RhB derived species.

5. CONCLUSIONS.

To conclude, the addition of g-C_3N_4 to $BiVO_4$ films successfully enhances their photocatalytic efficiency for the degradation of organic pollutants, due to the electron-hole pair separation, such as Rhodamine B, without altering the crystalline structure of the $BiVO_4$. The formation of a heterojunction between the two materials plays a key role in improving performance, enabling more efficient pollutant degradation while preserving the structural and functional properties of both components. This optimization demonstrates the potential of $BiVO_4$ – C_3N_4 composites in environmental remediation applications.

6. REFERENCES.

[1] A. E. Gahrouei, S. Vakili, A. Zandifar, and S. Pourebrahimi, “From wastewater to clean water: Recent advances on the removal of metronidazole, ciprofloxacin, and sulfamethoxazole antibiotics from water through adsorption and advanced oxidation processes (AOPs),” Environmental Research, vol. 252. Academic Press Inc., Jul. 01, 2024.

[2] H. Yang, “A short review on heterojunction photocatalysts: Carrier transfer behavior and photocatalytic mechanisms,” Mater Res Bull, vol. 142, p. 111406, Oct. 2021.

[3] Y. Park, K. J. Mc Donald, and K. S. Choi, “Progress in bismuth vanadate photoanodes for use in solar water oxidation,” Chem Soc Rev, vol. 42, no. 6, pp. 2321–2337, Feb. 2013.

[4] S. Hernández, G. Gerardi, K. Bejtka, A. Fina, and N. Russo, “Evaluation of the charge transfer kinetics of spin-coated $BiVO_4$ thin films for sun-driven water photoelectrolysis,” Appl Catal B, vol. 190, pp. 66–74, Aug. 2016.

[5] H. Dong, X. Guo, C. Yang, and Z. Ouyang, “Synthesis of g-C_3N_4 by different precursors under burning explosion effect and its photocatalytic degradation for tylosin,” Appl Catal B, vol. 230, pp. 65–76, Aug. 2018.